Mesoscale and high-frequency variability of macroscopic particles (> 100 μm) in the Ross Sea and its relevance for late-season particulate carbon export

Alexander B. Bochdansky[*1], Melissa A. Clouse[1], Dennis Hansell[2]

[1] Ocean, Earth and Atmospheric Sciences, Old Dominion University, Norfolk, VA, USA

[2] Department of Ocean Sciences, University of Miami, Miami, FL, USA

[*]corresponding author

Abstract:

The Ross Sea plays a major role in the transfer of organic carbon from the surface into the deep sea due to high productivity in that system. Here we present the first particle inventory (>100 μm) of the Ross Sea based on a combined deployment of a video particle profiler and a high-resolution digital holographic microscope. Long-distance (100s of kilometers) and short-distance (10s of kilometers) sections showed high variability of particle distributions that were dependent on the density structure of the water column. Particle export was especially apparent at sites of locally weakened pycnoclines. Similarly, *Phaecocystis antarctica* colonies that were initially retained in the mixed layer by a strong density gradient sank below the euphotic zone after erosion of the main pycnocline. Fine scale analysis at a resolution <1m revealed a significantly overdispersed (i.e., patchy) environment in all casts. Patchiness, as determined by the Lloyd index of patchiness and the Index of Aggregation, increased below the pycnocline presumably due to aggregation of particles while accumulating on density gradients. In contrast, particles in the upper mixed layer and in the nepheloid layers were more randomly distributed. In approximately half of the 84 video depth profiles, a periodicity of particle peaks was detectable, ranging from 10 to 90 m with a mode of 30 m, which can be regarded as the "relevant scale" or "characteristic patch size" of the vertical distribution of particles. We speculate that this banding of particles are sinking events that reflect cyclical weather patterns and changing wind speeds.

While chlorophyll fluorescence and particle mass determined by the video particle profiler were significantly correlated, the relationship changed from station to station and through time, reflecting changes in the relative contribution of fresh phytoplankton to total particle mass. Particles that sank below the main pycnocline were composed of diatoms, marine snow with and without embedded phytoplankton, crustacean plankton, and a surprisingly high percentage of heterotrophic (and perhaps mixotrophic) protists such as acantharians and tintinnids.

1. Introduction

The nutrient-rich Ross Sea is the site of massive seasonal blooms of phytoplankton (primarily diatoms and *Phaeocysystis antarctica*) and accumulation of dissolved and particulate organic carbon (Carlson et al. 2000, DiTullio et al. 2000). Particle export in the Ross Sea has commonly been measured with sediment traps (e.g., Asper and Smith 1999, Smith and Dunbar 1998, Accornero et al. 1999). The POC inventory of the water column has been measured on several expeditions using Niskin bottles and GF/F filters that capture all particulate matter > ~0.7 μm (e.g., Carlson et al. 2000). However, particles between 50 μm to several millimeters contribute most to the mass flux as smaller particles do not sink sufficiently fast, and larger particles are too rare to play a major role (Guidi et al. 2008, McDonnell and Buesseler 2010). The smallest particles in this size range are primarily composed of single diatom cells ballasted by their silica skeletons (McDonnell and Buesseler 2010). Surveys of these critical larger particles are much rarer, especially in the Ross Sea (Asper and Smith 2003). Since optical backscatter and beam transmissometry are more responsive to fine particles and colloidal material (Battisto et al. 1999, Bochdanksy et al. 2010), large particles are most efficiently measured by camera systems (Stemmann et al. 2000, Guidi et al. 2008, Iversen et al. 2010). In order to better understand the spatial and temporal distribution of macroscopic particles in the late season Ross Sea, we deployed a video particle profiler (VPP) in combination with a digital holographic microscope (DIHM).

2. Methods

2.1 Research expedition details

Data presented in this manuscript were collected on the RVIB *Nathaniel B Palmer* from February 12 to March 16, 2013. The main focus was on the western Ross Sea as it represents a significant site for Antarctic Bottom Water formation. During that time period, the Ross Sea transitioned from being almost entirely ice free to almost completely ice covered. We focused on three areas in the western Ross Sea: north of Franklin Island, South of Coulman Island, and Terra Nova Bay, each of which we revisited several times during the expedition in order to record temporal changes. We also sampled along 76° 30’S across the width of the Ross Sea.

2.2 Video particle profiler (VPP)

The VPP is similar to that published in Bochdansky et al. 2010. However, instead of lighting at 45° angle from both sides, side lighting with two white high-intensity LED lights was used ~7 cm in front of the lens. The light beams were restricted using a slit of 1 cm in width; however, as the light intensity dropped exponentially in the front and the back of the image beam, only the brightest lit image plane was used for analysis. This method reduced bias due to overlapping particles and provided more accurate particle size estimates. At the focal plane, the imaged area was 3 cm tall and 4 cm wide. The analysis program for the video particle profiler was expanded from that in Bochdansky et al. (2010) to include more variables for particle characterization (including perimeter, volume and porosity). The VPP can record 30 images per second, with image analysis by a Linux-based image analysis program (a converted Avidemux video editor) at high speeds (approximately in real time). The images were later aligned with depth from the CTD using time as the common variable and by filming a clock displaying UTC at the beginning and the end of each video sequence. In Matlab, CTD data were matched line-by-line with each set of the particle data. The raw data consisted of millions of particles each with its own set of associated CTD data. These raw data allow us to resample particle metrics at all possible scales. Particle volumes were calculated as shown in Fig. 1, avoiding the bias of assigning disproportionally large volumes to elongated objects. Total particle volume per meter depth interval was approximated by multiplying the mean volume of particles with the mean particle number at meter intervals, and expressed as parts per million (ppm) of the survey volume.

2.3 Digital inline holographic microscopy (DIHM)

Details of this method were published in Bochdansky et al. (2013). Briefly, a laser beam is focused on a 9 μm single-mode optical fiber that serves as a small but intense point source of light. The expanding beam intercepts particles that create interfering shadow images on the adjacent screen of a high-resolution (4.2 megapixel) CCD camera without lens. The camera was connected to an eBOX530-820-FL1.6G-RC computer (Axiomtek) with a Gb LAN cable that recorded images on a 750 GB hard disk at a frame rate of approximately 7-12 images per second. When the laser beam intercepts a structure, a portion of the image beam scatters and interferes with the light of the main beam in a predictable pattern. This raw image represents a hologram that can then be reconstructed applying the Kirchhoff–Helmholtz transform (Xu et al. 2001) and using commercially available reconstruction software (Octopus, 4-Deep Inwater Imaging, formerly Resolution Optics). Being lens-less, the advantage of this method is that anything in the image beam can be reconstructed without having to rely on the focal plane of a lens. The entirety of the image beam volume (i.e., 1.8 ml in this configuration) can be reconstructed in this fashion, and thus explores orders of magnitude more volume than a lens-based system at the same resolution. Reconstruction of the images and analysis (particle quantities and sizes and type) were performed manually as no reliable image reconstruction and analysis system exists for the DIHM at this time. In the future, several tens of thousands of these hand-reconstructed holograms will be used for validation and calibration for automated systems. The DIHM can detect hard structures (e.g., silica, chitin, calcium carbonate, strontium sulfate) to a resolution as small as 5 μm, and reliably count particles of 50 μm to ~8 mm in the image volume (Bochdansky et al. 2013).

In the VPP, particle numbers cannot be directly assigned to a defined image volume because of the diffuse border of the unconstrained light beam and the fact that different particle types have different reflectivities. In contrast, the DIHM provides very accurate and precise image volumes and number of particles within the laser image beam. For these reasons, the VPP was calibrated with the DIHM at 11 stations over 10-20 m depth ranges. The conversion factor to apply to the video images was:

(equation 1) $N_v = N_{dihm} \times 0.244$ (n=11 stations, SD = 0.097), where N_v = number of particles > 100 μm per video frame, and N_{dihm} the number of particles > 100 μm per ml as determined by the DIHM. In other words, each video frame corresponds to 4.1 ml sample volume. In contrast to the DIHM, the VPP provides a high throughput system that allows for much greater coverage.

The degree of overdispersion (i.e., patchiness) in the system was assessed using two indices. One, the Lloyd index of patchiness (Lloyd 1967), is domain-dependent (i.e., zero values affect the estimates); the other one, the index of aggregation, is domain-independent (Bez 2000). The Lloyd index (Lloyd 1967) was calculated as:

(equation 2) $$lp = \left[m + \left(\frac{\sigma^2}{m} - 1\right)\right] m^{-1},$$

where *lp* is the Loyd index of patchiness, *m* the mean particle density, and σ^2 the variance of the particle density.

The index of aggregation (Bez 2000) was calculated as:

(equation 3) $$ia = \sum_i z_i^2 \, [S \times (\sum_i z_i)^2]^{-1},$$

where *ia* is the index of aggregation, z_i the particle density, and *S* the sample scale (set to 1 for this analysis).

Salinity, temperature, and oxygen measurements were obtained using a SeaBird 911+ conductivity, temperature, and depth (CTD) probe. Salinity samples were calibrated on discrete samples at 24°C using a Guildline 8400 Autosal four-electrode salinometer. A Seabird SBE 43 polarographic oxygen sensor and a Wetlabs ECO-FL fluorometer provided data on oxygen and chlorophyll fluorescence, respectively.

All raw data from the VPP and the DIHM, including the CTD context data, were archived at BCO-DMO (http://www.bco-dmo.org/), cross-listed under the name of the principal investigator

(Bochdansky) and the NSF research cruise number (NBP13-02). [Note to reviewers: We also requested archiving all the high-resolution DIHM images of which only a very small percentage have been manually reconstructed. These images represent a unique record of late-season standing stock in the Ross Sea, and could be used by investigators for future exploration of different depth ranges or taxonomic groups. In essence, they are records of micro- and mesoplankton distribution without being exposed to the decay in formaldehyde or Lugol's and at much higher spatial resolution than historical plankton samples. Automatic image analyses may also come online soon so that these images can be processed at much higher speed. Because of the many terabytes of storage requirements, our request is currently being reviewed by BCO-DMO staff]

2.4 Plankton identification using the DIHM

For detailed examination of particles and identification of plankton, we studied only depths at and below the pycnocline. The configuration of the DIHM was intended to maximize image volume and to target particles deeper in the water column (i.e., those that contribute to export flux). For surveys of surface plankton, a much smaller gap size would have to be chosen. The sequence was run and stopped when a larger particle was encountered (approximately >20% of the screen). In this fashion all large particles (> 100 μm) were captured but also smaller particles that are closer to the point source of the laser beam. These smaller particles were excluded from quantitative analysis later. The maximum length was determined using the measuring tool of the Octopus reconstruction software. This result was converted to a corrected length based on object distance from the camera. The 100 μm threshold corresponds well with the approximate minimum particle size as seen by the video camera. *Phaeocystis* colonies, because of their dense structure, do not reconstruct very well; however, they have a very characteristic shape and texture even in the unreconstructed holograms (Fig. 2). We were therefore able to perform a detailed analysis on them on all casts through all depths, but excluded them from analysis in the more restricted depth ranges (see above).

Section plots were created using Ocean Data View (Schlitzer 2015).

3. Results and Discussion

The emphasis of this late-season survey was on three areas in the western Ross Sea (Terra Nova Bay, south of Coulman Island, and north of Franklin Island), which were revisited several times during the research expedition to obtain information on temporal changes of the system. Terra Nova Bay was the site of highest drawdown of CO_2 of all sites visited (DeJong et al., 2015). We also performed short-distance transects to obtain insight on the high-resolution spatial variability, and one long-distance zonal transect across the Ross Sea at the 76° 30'S line, a section visited during previous research cruises (e.g., Carlson et al. 2000, Smith et al. 2013)

3.1 Long-distance transect at the 76° 30' line

Using the first derivative of potential density (referred to here as sigma theta') provided insights into the strength of the density discontinuities. Along the transect, the main pycnocline was weaker in some areas than others (i.e., the bands of sigma theta' were narrower and vertical density gradients weaker). At these sites, increased particle numbers were observed at depth and frequently appeared in bands (arrows in Fig. 3). This result was a consistent pattern along the entire 76° 30'S line, although surface salinity decreased continuously eastwards. This outcome confirms that relative density changes are more important for sinking and aggregation of particles than absolute density values. Layers of marine snow and thin layers of phytoplankton are often associated with strong pycnoclines where particle maxima can be found in or just below the most pronounced density discontinuity (MacIntyre et al. 1995, Dekshenieks et al. 2001). Total particle volume (ppm) was also increased in the nepheloid layer in a broad band above the ocean bottom. Apparent oxygen utilization (AOU) increased sharply below the main pycnocline as a result of oxygen-enriched surface water not being mixed below the density gradient as well as oxygen consumption of deep particle-associated heterotrophs (Fig. 3). The highest AOUs also coincided with the distribution of the largest particles, indicating that oxygen consumption was highest at sites where marine snow was found in large quantities (Fig. 3). Patchiness as indicated by the Lloyd index was highly variable throughout the water column, with highest values generally at stations and depths at which particle abundance was low. In some spots, extremely high values coincided with the largest mean particle sizes (Fig. 3).

3.2 North of Franklin Island short transect

This transect provided some insights into more highly resolved spatial variability of the Ross Sea system. Again, high particle mass in the surface was associated with a weakened pycnocline, likely the result of mixing of nutrients to the surface and a localized bloom (Fig. 4). Increased particle mass at depth was the result of a combination of high particle load at the surface and the lessened density barrier. This finding suggests that particle export this late in the season is highly episodic in nature. A strong pycnocline in one portion of the transect kept particles suspended at and just below the density gradient (left side in Fig. 4), contributing greatly to the high AOUs there (Fig. 4). Particle size increased at and just below the pycnocline likely as a result of aggregation (Alldredge et al. 2002).

3.3 South of Coulman Island

A massive particle export was apparent in bands at one station in the center of the line that coincided with a weak pycnocline (Fig. 5a, arrow). However, in one portion of the transect (to the left in Fig. 5), strong particle peaks were present at depth (Fig. 5b) despite a rather strong density gradient at the main pycnocline (Fig. 5a).

3.4 Fine-scale distribution

High-resolution and high-frequency analysis of particles by the VPP allowed us to explore submeter patchiness. These very small scales are highly relevant for plankton dynamics and biophysical processes (Wolk et al. 2004). Our analysis was based on individual frames collected at a frame rate of 30 per second, each of which surveys approximately 4 ml of seawater. This meant that the scale of our fine-scale analysis was well below 1 m. Whether or not particle distributions at this scale were significantly overdispersed was tested by comparing the frequency distribution of particle counts with a standard Poisson distribution. Particle distributions were significantly overdispersed ($p<0.005$) in all profiles at these small scales, especially below the pycnocline and above the nepheloid layer. The two indices (the index of aggregation and the Lloyd index of patchiness) showed similar trends, but they were also markedly different from each other (Fig. 6). Sometimes the relationship bifurcates; the IA seems to flatten where the Lloyd index shows large deviations at higher values (Fig. 6). We therefore conclude that the Lloyd index is a better metric in describing highly overdispersed micropatches. A Lloyd index of 1 reflects a random distribution of particles as was the case in the presence of finely suspended material such as found in the upper mixed layer and in the bottom nepheloid layer (Fig. 3 and 4). When subsampling the same data over increasingly larger spatial scales (1 m, 3 m, 5 m, 11 m, etc.), the Lloyd index of patchiness quickly approached values close to one, indicating a more random distribution of particles at these larger scales (not shown). Arbitrary binning into larger and larger depth intervals, however, misses the periodicity that was apparent in the particle peaks through the water column. For this reason, we tested for periodicity by using fast Fourier transforms (FFT) for each cast. Of 84 casts, 40 showed a clear peak in the periodogram after a FFT (example in Fig. 7b). Casts that did not show periodicity of smaller particle peaks often displayed one or two very prominent peaks indicative of large settling events (Fig. 7c). For casts with detectable periodicities, average peak-to-peak distances ranged from 10 to 90 m with the most frequent bin of 30 m (Fig. 8). These periodicities can be interpreted as the "characteristic patch size" for particle peaks (> 100 μm). Given the relevance of a continuum of temporal and spatial scales to phytoplankton growth (Harris 1980), even small observed periodicities require overwhelming physical or biological forcing mechanisms. In other words, even subtle observed frequencies may indicate very strong causes. While intriguing, it is unclear what caused the observed periodicity in particle peaks. These peaks either were the result of water column density structure (i.e., particles being retained at local pycnoclines), or of episodic sinking events, or both. Smith et al. (2010) observed high temporal variability of fluorescence in surface water that they attributed to wind-induced advective changes. It is thus possible that periodicity in weather patterns would lead to the observed periodicities in particle peaks with depth. This forcing would be in addition to factors known to control export such as surface production and grazer community composition (Smith and Dunbar 1998).

The relationship between particle data and fluorescence signal was also investigated. Fluorescence and ppm were correlated albeit at low r^2 values (Fig. 9). At some stations, the ppm and fluorescence data were tightly coupled (Fig. 9a), while at other stations the variables diverged widely (Fig. 9b). A relatively tight coupling between fluorescence and total particle volume may be indicative of fresh phytoplankton dominating overall particle mass (Fig 9a). At other stations, the two signals were more decoupled, showing a flattening of the relationship especially at lower particle number ranges (i.e., the ranges that are most important to estimate fluxes below the primary pycnocline). One location that was probed at 2 week intervals (casts 55 and 104) not only revealed a more variable relationship between total particle volume and fluorescence but also displayed significant differences in slopes and elevations of the regression lines over the two week interval (ANCOVA, $n = 656$, homogeneity of slopes: $F = 1179$, $p \ll 0.0001$; elevation: $F=339.6$, $p \ll 0.0001$, Fig. 9b). Changes in the relationship between fluorescence and the total particle volume as detected by video images may thus be useful as indicators for the relative state of degradation of particulate matter, assuming that fresh phytoplankton material at the surface would have the highest fluorescence relative to particle volume, while particles dominated by heterotrophs, marine snow mucous matrix, and more refractory phytoplankton would show lower fluorescence-to-particle volume ratios. The observed decrease in fluorescence at a given particle volume later in the season is consistent with this trend (Fig. 9b).

3.5 Particle composition and plankton distributions

At 26 stations we examined the composition of large particles using the DIHM from the center of the main pycnocline downwards. For this analysis, only particles >100 µm were considered because taxonomic interpretation of smaller particles is exceedingly difficult even with the DIHM. The particles were grouped into five categories: marine snow, phytoplankton, zooplankton, unidentified organisms, others (Fig. 10 and 11). Marine snow included amorphous aggregates, clusters, stringers, and aggregates containing organisms (Fig. 10). Phytoplankton included *Rhizosolenia* spp (30% of total phytoplankton observed), *Corethron* spp (7%), *Chaetoceros* spp (0.2%), other diatoms, and dinoflagellates (0.1%) (Fig. 10). Analysis of *Phaeocystis* was performed separately and in more detail (see below). Zooplankton included acantharians (52% of total zooplankton observed), copepods (24%), tintinnids (9%), larvaceans (7%), and nauplii (5%) (Fig. 10). Unidentified organisms included particles clearly organismal but that could not be classified with certainty. “Others” included optically dense singular particles that did not classify as marine snow or organismal; some of them could have been large fecal pellets.

As expected, many of the larger particles were composed of marine snow that were either amorphous with unidentifiable content, or contained large numbers of aggregated diatoms (Fig. 11). Particles below the main pycnocline were composed of a surprisingly large number of zooplankton, and because they cannot migrate back into the mixed surface layer (except for the largest copepods), they become part of the export flux. Acantharians as well as ciliates, radiolarians, and foraminifera are known for kleptoplasty (Stoecker et al.2009), therefore there is some overlap in the zooplankton and phytoplankton categories. Among ciliates, only loricate forms image well with the DIHM, which means that the total ciliate numbers would have to be ~10 times higher when accounting for the much more numerous aloricate ciliates (Assmy et al. 2013 PNAS supplementary section Fig. 53). The lack of Radiolaria and Foraminifera in our samples was remarkable given the fact that they should produce good images with the DIHM. This result means that among Cercozoa (including former Radioloaria) and Retaria (including Foraminifera and Acantharia, Adl et al. 2005), Acantharia make up the bulk mass. These organisms were historically underestimated as they are lost with conventional preservation methods (Beers and Stewart 1970).

3.6 *Phaeocystis antarctica* colony distribution

P.antarctica (Haptophyta) colonies were very common at some stations in the western Ross Sea but remarkably confined to a region between 169° and 190°E (Fig. 13). This distribution corresponds well with the highest abundance levels observed in DiTullio et al. (2000) for earlier parts of the seasonal growth cycle. The abundance levels were highest at station # 15 followed by station # 121 (Fig. 13) both in terms of average numbers of *Phaeocystis* colonies and as integrated over the entirety of the mixed layer (Fig. 12). Over a period of two weeks, we observed sinking of a large number of colonies from the surface mixed layer through the pycnocline into the deeper layer where *Phaeocystis* colonies can be considered to have been undergone export. This penetration of *Phaeocystis* into deep water was associated with a marked weakening of the pycnocline during the same period (Fig. 14). Thus *Phaeocystis* colonies not only contribute significantly to total export production during the main growing season in the Austral spring and summer (DiTullio et al. 2000) but also in the fall. Our observations, showing retention on strong pycnoclines followed by significant export, however, suggests that export is highly episodic, consistent with previous sediment trap observations (Smith and Dunbar 1998).

4. Conclusions

Spatial and temporal variability of particles >100 µm is very high in the autumnal Ross Sea at all measured scales. We observed a characteristic banding pattern in the microscale distribution of particles at characteristic scales of tens of meters. These bands likely reflect sinking events as a result of cyclical wind events that locally erode the main pycnocline and allow particles to sink into deeper strata. Analysis of DIHM images revealed a large contribution of live or moribund plankton below the pycnocline, which represent a source of undegraded carbon for deeper layers. Fluorometry cannot reliably determine particle mass through the water column, not only because of the limit of detection but also because of the fact that the relationship between total particle volume and fluorescence changes spatially and temporally. In turn, a tight coupling between total particle volume and fluorescence may indicate a large contribution of fresh phytoplankton to sinking fluxes.

Acknowledgements: We would like to thank our Co-PIs on this project Robert Dunbar, Jack DiTullio, Monica Orellana. Cody Garrison helped with the deployment of the DIHM and the VPP. We also thank the crew and the Polar Program scientific support team of the RV Nathaniel B Palmer. This project was funded by the National Science Foundation, Division of Polar Program grants #1142097 to ABB, and # 1142117 to DAH.

References

Accornero A, Bergamasco A, Monaco A, Tucci S. 1999. Particle fluxes at the edge of the Ross Ice Shelf: the role of physical forcing. Oceanography of the Ross Sea Antarctica, eds Spezie G, Manzella GMR (Springer, Milan), pp177-195.

Adl SM, Simpson AGB, Farmer MA et al. 2005. The new higher level classification of eukaryotes with emphasis on the taxonomy of protists. J. Eukaryot. Microbiol. 52(5), 399-451.

Alldredge, AL, Cowles TJ, MacIntyre S et al. 2002. Occurrence and mechanisms of formation of a dramatic thin layer of marine snow in a shallow Pacific fjord. Mar Ecol Prog Ser. 233, 1-12.

Asper VL, Smith WO. 1999. Particle flux during austral spring and summer in the southern Ross Sea, Antarctica. J. Geophys. Res. 104, C3, 5345-5359.

Asper VL, Smith WO. 2003. Abundance, distribution and sinking rates of aggregates in the Ross Sea, Antarctica. Deep-Sea Res. I, 50, 131-150.

Assmy P, Smetacek V, Montresor M et al. 2013. Thick-shelled, grazer-protected diatoms decouple ocean carbon and silicon cycles in the iron-limited Antarctic Circumpolar Current. PNAS. 110(51), 20633-20638.

Battisto GM, Friedrichs CT, Miller HC, Resio DT. 1999. Response of OBS to mixed grain size suspensions during SandyDuck ’97. Coastal Sediments: Proceedings of the International Symposium on Coastal Engineering and Science of Coastal Sediment Processes, eds Kraus NC, McDougal WG (Hauppauge, Long Island, New York), pp297–312.

Beers JR, Stewart GL. 1970. The preservation of acantharians in fixed plankton samples. Limnol. Oceanogr. 15(5), 825-827.

Bez N. 2000. On the use of Lloyd’s index of patchiness. Fish. Oceanogr. 9(4), 372-376.

Bochdansky ABB, Jericho MH, Herndl GJ. 2013. Development and deployment of a point-source digital inline holographic microscope for the study of plankton and particles to a depth of 6000m. Limnol. Oceanogr. Methods. 11, 28-40.

Bochdansky ABB, van Aken HM, Herndl GJ. 2010. Role of macroscopic particles in deep-sea oxygen consumption. PNAS. 107(18), 8287-8291.

Carlson CA, Hansell DA, Peltzer ET, Smith Jr WO. 2000. Stocks and dynamics of dissolved and particulate organic matter in the southern Ross Sea, Antarctica. Deep-Sea Res. II 47, 3201-3225.

DeJong HB, Dunbar RB, Mucciarone D, Koweek DA. 2015. Carbonate saturation state of surface waters in the Ross Sea and Southern Ocean: controls and implications for the onset of aragonite undersaturation, Biogeosciences 12, 6881-6896.

Dekshenieks MM, Donaghey PL, Sullivan JM et al. 2001. Temporal and spatial occurrence of thin phytoplankton layers in relation to physical processes. Mar. Ecol. Prog. Ser. 223, 61-71.

Guidi L, Jackson GA, Stemmann L et al. 2008. Relationship between particle size distribution and flux in the mesopelagic zone. Deep-Sea Res. 1. 55, 1364-1374.

Harris GP. 1980. Temporal and spatial scales in phytoplankton ecology. Mechanisms, methods, models, and management. Can. J. Fish. Aquat. Sci. 37, 877-901.

Iversen MH, Nowald N, Ploug H, Jackson GA, Fischer G. 2010. High resolution profiles of vertical particulate organic matter export off Cape Blanc, Mauritania: Degradation processes and ballasting effects. Deep-Sea Res. 1. 57, 771-784.

Kirchman DL, Moran XAG, Ducklow H. 2009. Microbial growth in the polar oceans - role of temperature and potential impact of climate change. Nature Reviews Microbiology. 7, 451-459.

Lloyd M. 1967. Mean crowding. J. Anim. Ecol. 36, 1-30.

Lutz M, Dunbar R, Caldeira K. 2002. Regional variability in the vertical flux of particular organic carbon in the ocean interior. Global Biogeochemical Cycles. 16(3), 11-1-15.

MacIntyre S, Alldredge AL, Gotschalk CC. 1995. Accumulation of marine snow at density discontinuities in the water column. Limnol. Oceanogr. 40(3), 449-468.

McDonnell AMP, Buesseler KO. 2010. Variability in the average sinking velocity of marine particles. Limnol. Oceanogr. 55(5), 2085-2096.

Schlitzer, R., 2015. Ocean Data View, http://odv.awi.de

Smith Jr WO, Asper V, Tozzi S et al. 2011. Surface layer variability in the Ross Sea, Antarctica as assessed by in situ fluorescence measurements. Progress in Oceanography. 88, 28-45.

Smith Jr WO, Dunbar RB. 1998. The relationship between new production and vertical flux on the Ross Sea continental shelf. J. Mar. Sys. 17, 445-457.

Smith Jr WO, Tozzi S, Long MC et al. 2013. Spatial and temporal variations in variable fluorescence in the Ross Sea (Antarctica): Oceanographic correlates and bloom dynamics. Deep-Sea Res. I. 79, 141-155.

Stoecker D. K., Johnson M. D., De Vargas C., Not F. (2009). Acquired phototrophy in aquatic protists. Aquat. Microb. Ecol. 57, 279–310

Stemmann L, Picheral M, Gorsky G. 2000. Diel variation in the vertical distribution of particulate matter (>0.15 mm) in the NW Mediterranean Sea investigated with the Underwater Video Profiler. Deep-Sea Res. 1. 47, 505-531.

Tang KW, Smith Jr WO, DT Elliott, AR Shields. 2008. Colony size of Phaeocystis Antarctica (Prymnesiophyceae) as influenced by zooplankton grazers. J. Phycol. 44, 1372-1378.

Wolk F, Seuront L, Yamazaki H et al. 2004. Comparison of biological scale resolution from CTD and microstructure measurements. In: Handbook of Scaling Methods in Aquatic Ecology: Measurement, Analysis, Simulation, Seuront L et al (ed), 3-15.

Xu W, Jericho MH, Meinertzhagen IA et al. 2001. Digital in-line holography for biological applications. PNAS. 98(20), 11301-11305.

Figure legends:

Fig. 1. Method for approximating particle volumes. Image analysis determines the projectional area of an irregularly shaped particle with length *L*. This area is used to determine the equivalent spherical diameter (*ESD*) of a circle with the same area, which in turn is used to determine the volume of a sphere of the same diameter. The advantage of this method is that the area is dimensionally only once removed from volume, and some of the irregularities of objects are accounted for.

Fig. 2. Unreconstructed holographic image of a *Phaeocystis antarctica* colony. Diameter of *P. antarctica* colonies varied from ~70 – 140 μm (Tang et al. 2008).

Fig. 3. Long-distance transect along the 76° 30'S line (West to the left). Variables from top to bottom are: (a) the first derivative of sigma theta (sigmaΘ') indicating the strength of the pycnocline, (b) the mean particle volume as the product of mean particle abundances and mean particle volume at each meter of depth (unit: ppm), (c) the apparent oxygen utilization (unit: μmol kg^{-1}), (d) the Lloyd index of patchiness calculated according to equation 2 (at a random distribution of particles Lloyd index = 1), (e) relative mean volume of particles (cubic pixel). Arrows indicate weakening of the main pycnocline concomitant with bands of exported particles at depth.

Fig. 4. Short-distance section north of Franklin Island (west to east direction). (a) the first derivative of sigma theta (sigmaΘ') indicating the strength of the pycnocline, (b) the mean particle volume as the product of mean particle abundances and mean particle volume at each meter of depth (unit: ppm), (c) the apparent oxygen utilization (unit: μmol kg^{-1}), (d) the Lloyd index of patchiness calculated according to equation 2 (at a random distribution of particles

Lloyd index = 1), (e) relative mean volume of particles (cubic pixel). Arrows indicate weakening of the main pycnocline concomitant with bands of exported particles at depth.

Fig. 5. Short-distance section south of Coulman Island (northwest to southeast direction). (a) the first derivative of sigma theta (sigmaΘ’) indicating the strength of the pycnocline, (b) the mean particle volume as the product of mean particle abundances and mean particle volume at each meter of depth (unit: ppm), (c) the apparent oxygen utilization (unit: μmol kg^{-1}), (d) the Lloyd index of patchniess calculated according to equation 2 (at a random distribution of particles Lloyd index = 1). Arrows indicate weakening of the main pycnocline concomitant with bands of exported particles at depth.

Fig. 6. Three representative examples of the relationship between the Index of Aggregation (Bez 2000) and the Lloyd index of patchiness (Lloyd 1967) at submeter scales (~ 3.3 cm). A Lloyd index of 1 means that particles are randomly distributed, which most frequently occurred in the surface mixed layer. In some casts a bifurcation of the two indices was apparent (a). At higher levels of overdispersion, the Lloyd index shows a stronger numerical response than the Index of Aggregation, which means it is more sensitive to detecting patchy distributions of particles in the water column.

Fig. 7. Depth distribution of particle numbers (means per meter) versus depth (m). The inserts show the periodogram power spectral densities after fast Fourier transformation. (a) Example with no periodicity. (b) The most frequently encountered case (40 of 84casts), in which a periodicity was detectable at depth intervals shown in Fig. 8. (c) A large subsurface particle peak in some casts masked possible underlying periodicities at higher frequencies.

Fig. 8. Frequency distribution of peak periodicity of all casts (n=40) that had a detectable frequency in the particle distribution through the water column. In one fourth of the peaks in the

FFT periodogram (i.e., the basic modulus-squared of the discrete Fourier transform, n=10), the peak fell in the 30 m depth bin. This means that particle peaks occurred repeatedly at ~30 m depth intervals in the water column.

Fig. 9. Total particle volume at two locations in the Ross Sea and at two points in time (black vs green symbols). (a) Good agreement between total particle volume and fluorescence indicating that fresh phytoplankton dominate the flux. (b) More variable relationship between total particle volume and fluorescence that also changed significantly over a period of 2 weeks.

Fig. 10. Examples of DIHM used in our analysis. (a-c) stringer-type marine snow particles, (d-e) amorphous marine snow particles held together by optically transparent exopolymers, (f-g) diatoms embedded in marine snow, (h) *Corethron* spp., (i-j) chain forming diatoms, (k) *Rhizosolenia* sp., (l-m) acantharians, (n-o) tintinnids, (p) copepod, (q) *Fritillaria* sp., (r) nauplius, (s) crustacean carcass, (t) krill fecal pellet.

Fig. 11. Pie charts of the relative contribution of various particle groups to total particle numbers below the pycnocline. We consider these particles exported as only the largest zooplankton (too rare to be accounted for by the DIHM) would be able to swim back into the upper mixed layer.

Fig. 12. Mean (numbers liter^{-1}) (a) and integrated (m^{-2}) (b) abundance of *Phaeocystis antarctica* colonies as determined by the DIHM. Numbers in (a) represent the depths of the mixed layer at each site.

Fig. 13. *Phaeocystis antarctica* colony abundances (numbers liter^{-1}) along a section of the Ross Sea.

Fig. 14 Vertical distribution of *Phaeocystis antarctica* colonies (numbers liter^{-1}) in relation to sigmaΘ. *P. antarctica* colonies reached much deeper when the density gradients eroded (c and d) approximately 2 weeks later. The red lines represent 15 m moving averages.

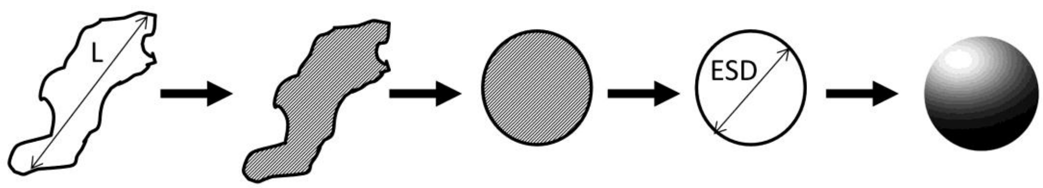

Fig. 1

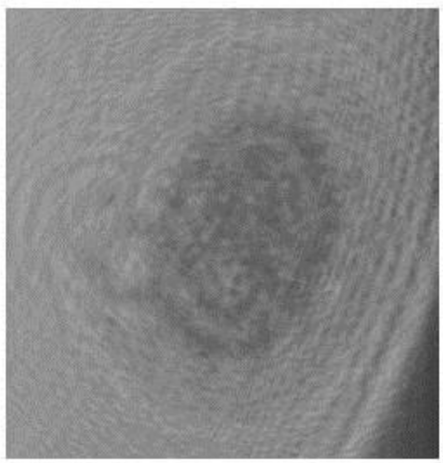

Fig. 2

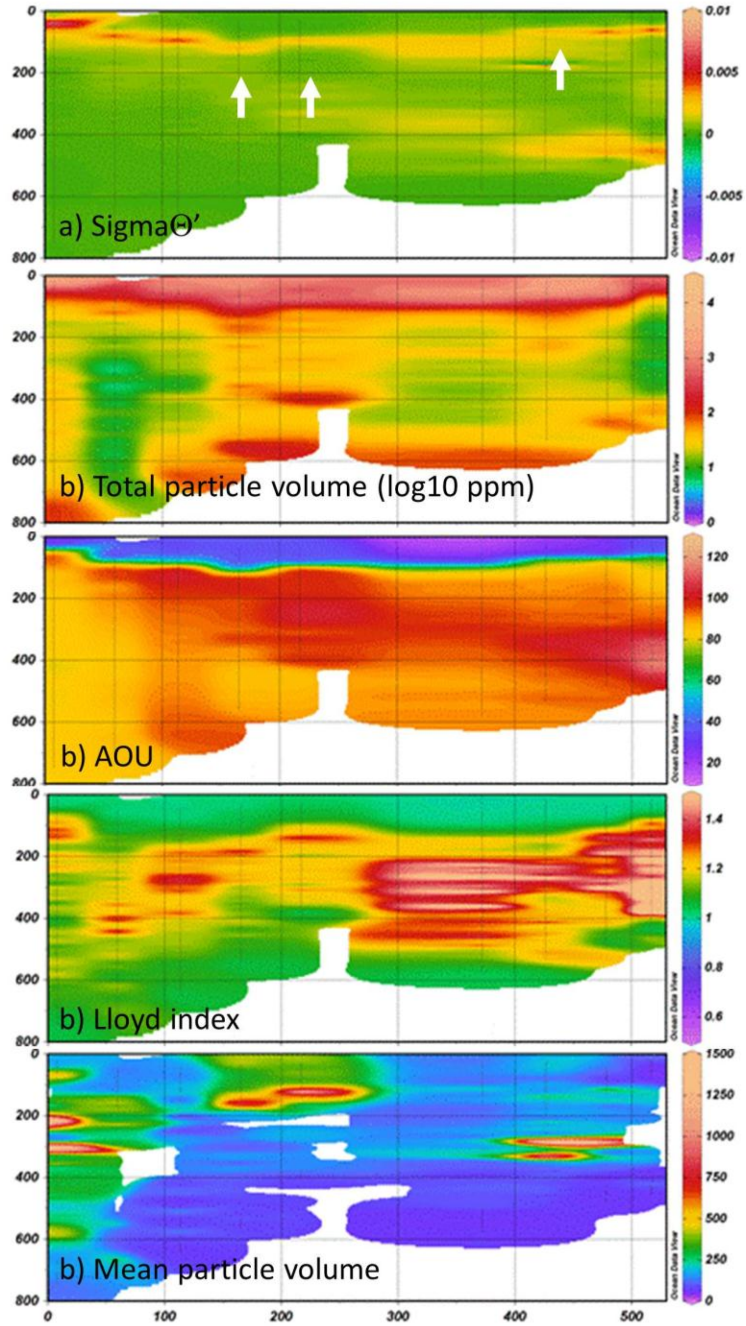
a) SigmaΘ'
b) Total particle volume (log10 ppm)
b) AOU
b) Lloyd index
b) Mean particle volume
0
100
200
300
400
500
600
800

Fig. 3

504

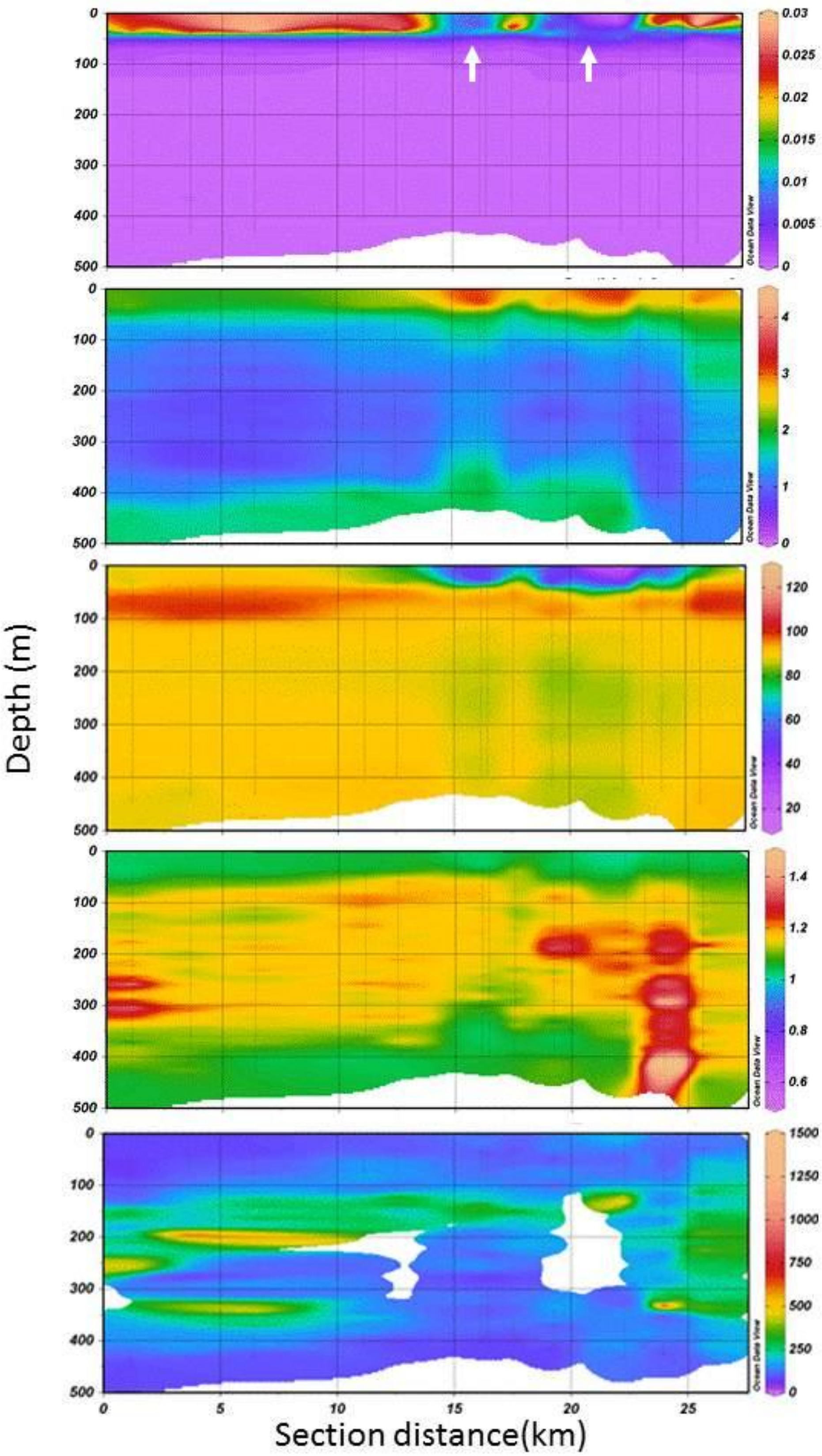

505

Fig. 4

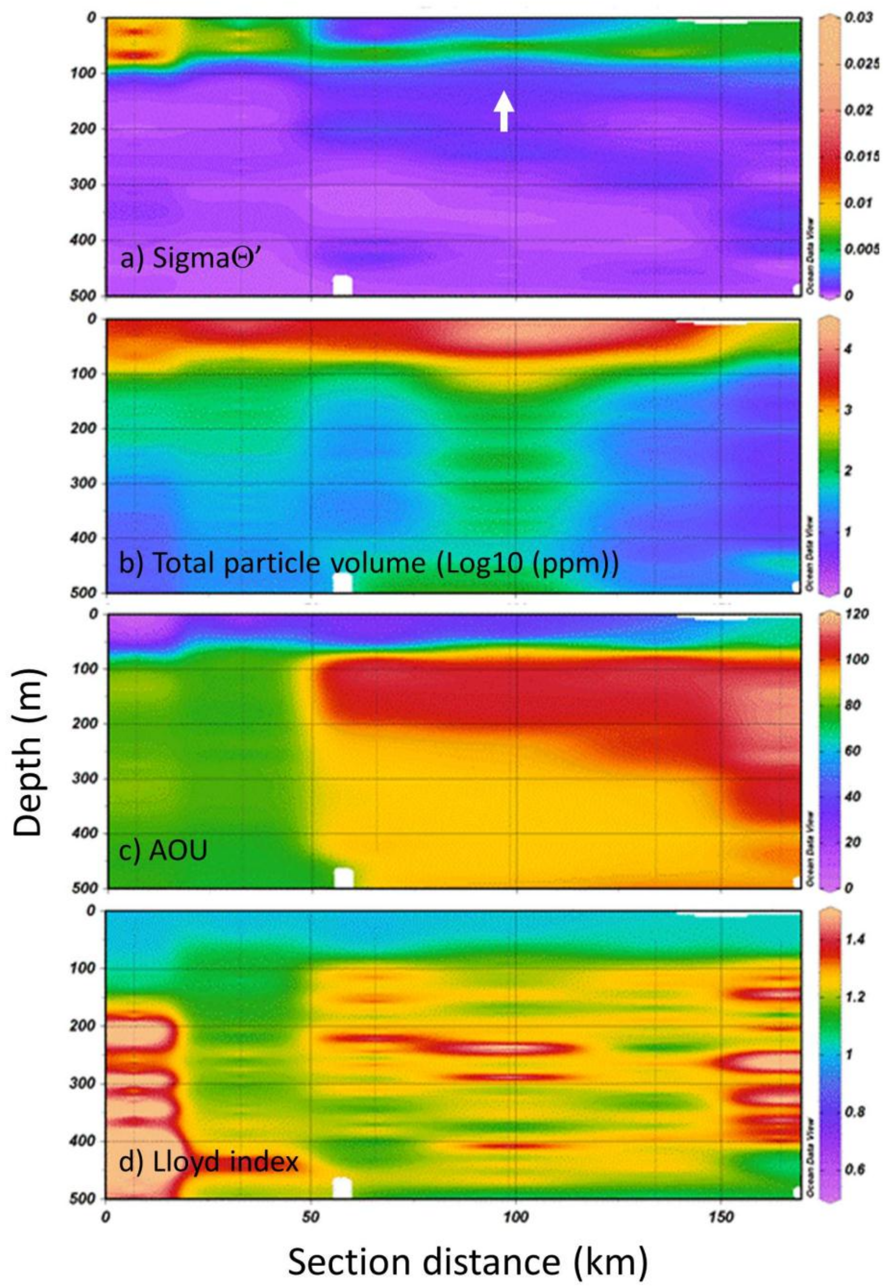
a) SigmaΘ'
b) Total particle volume (Log10 (ppm))
c) AOU
d) Lloyd index
Depth (m)
Section distance (km)
0
100
200
300
400
500
0
50
100
150
0.03
0.025
0.02
0.015
0.01
0.005
4
3
2
1
120
100
80
60
40
20
1.4
1.2
1
0.8
0.6
Ocean Data View

Fig. 5

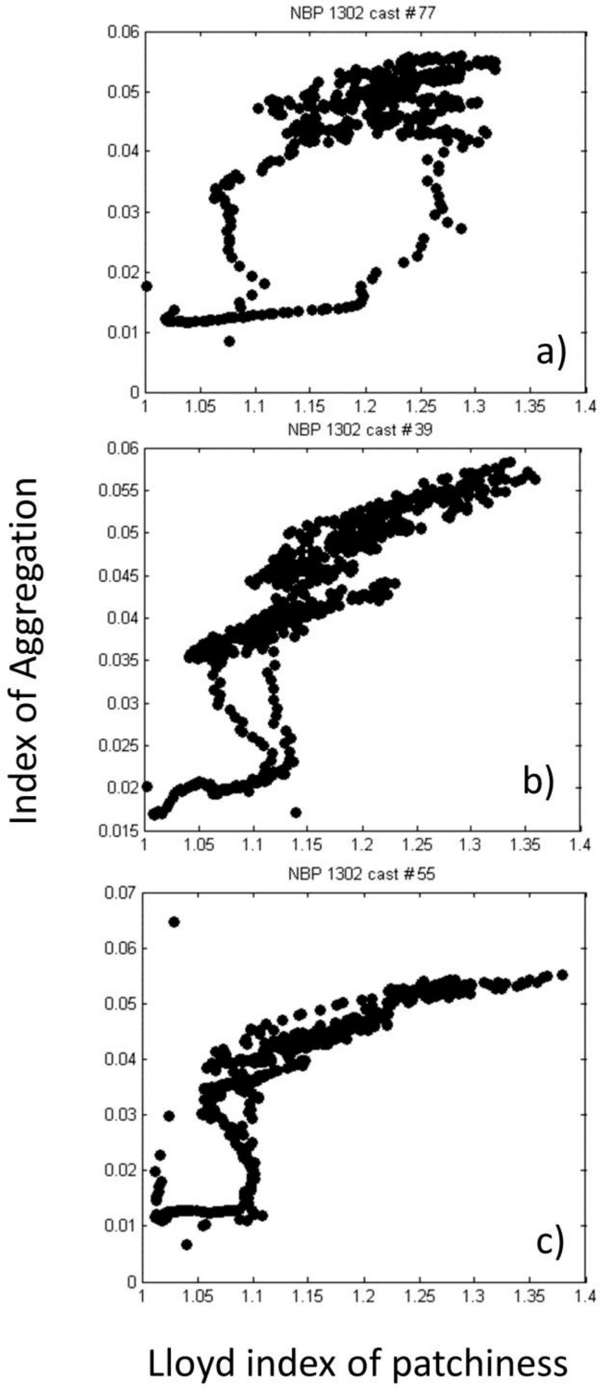
NBP 1302 cast #77
a)
NBP 1302 cast #39
b)
NBP 1302 cast #55
c)
Index of Aggregation
Lloyd index of patchiness

Fig. 6

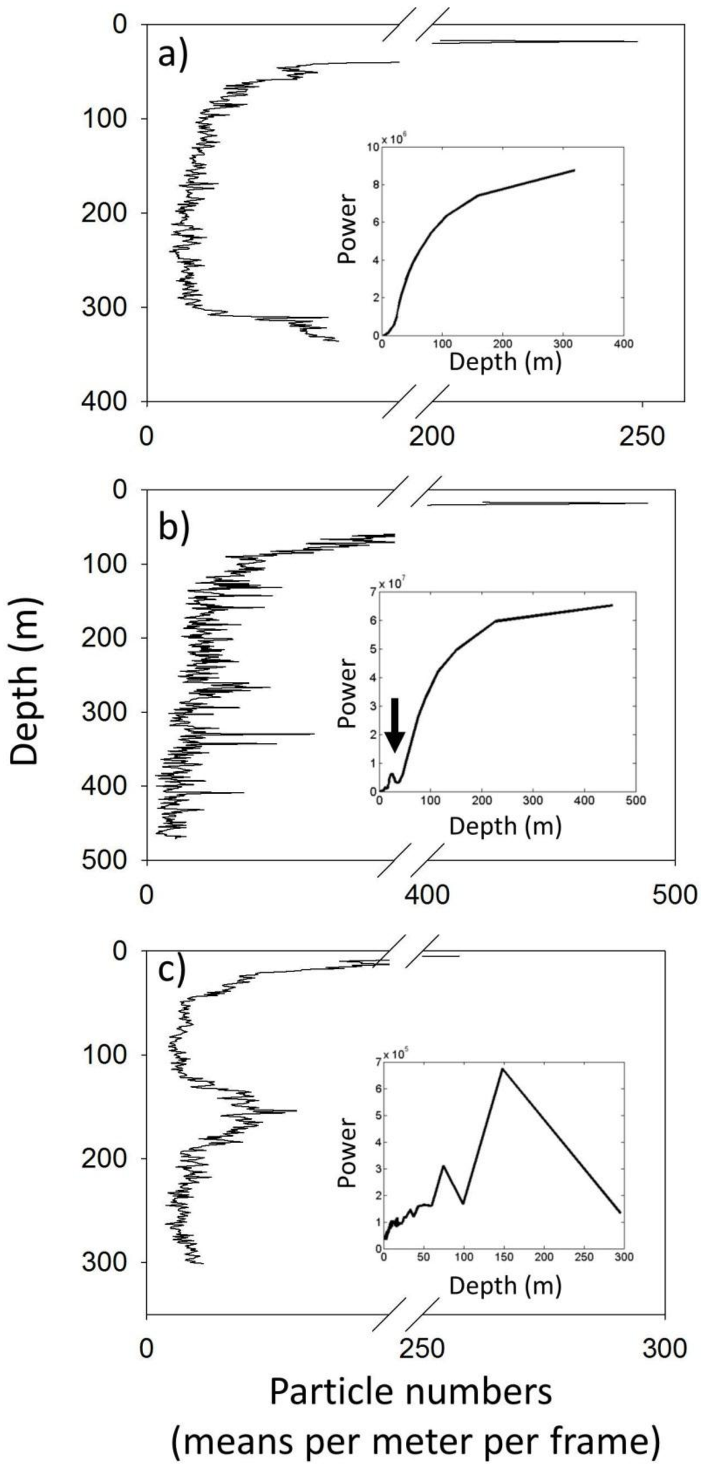

a)
b)
c)
Depth (m)
Power
Particle numbers
(means per meter per frame)

Fig. 7

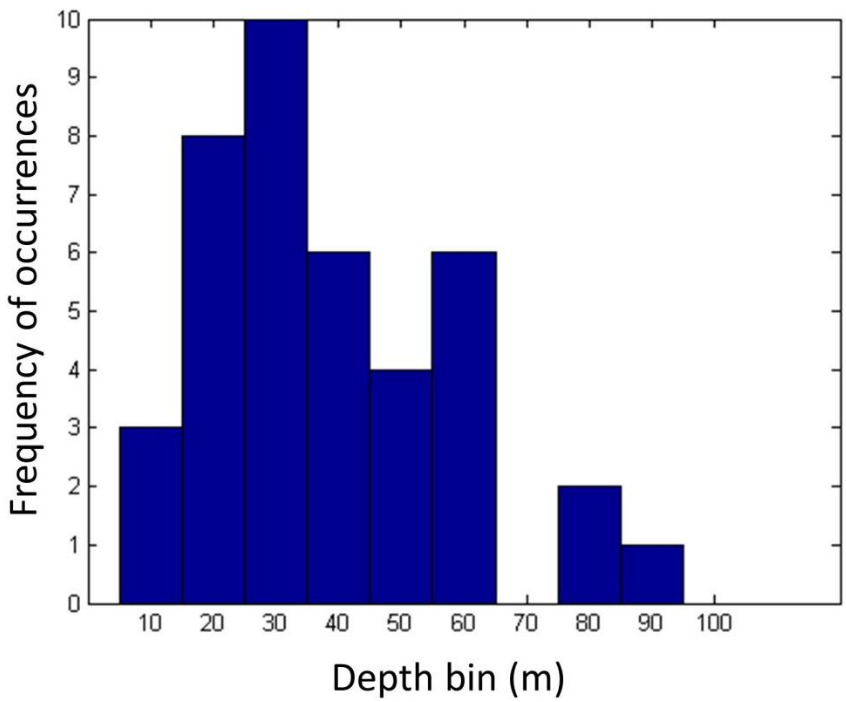
Frequency of occurrences
Depth bin (m)
0
1
2
3
4
5
6
7
8
9
10
10
20
30
40
50
60
70
80
90
100

Fig. 8

509

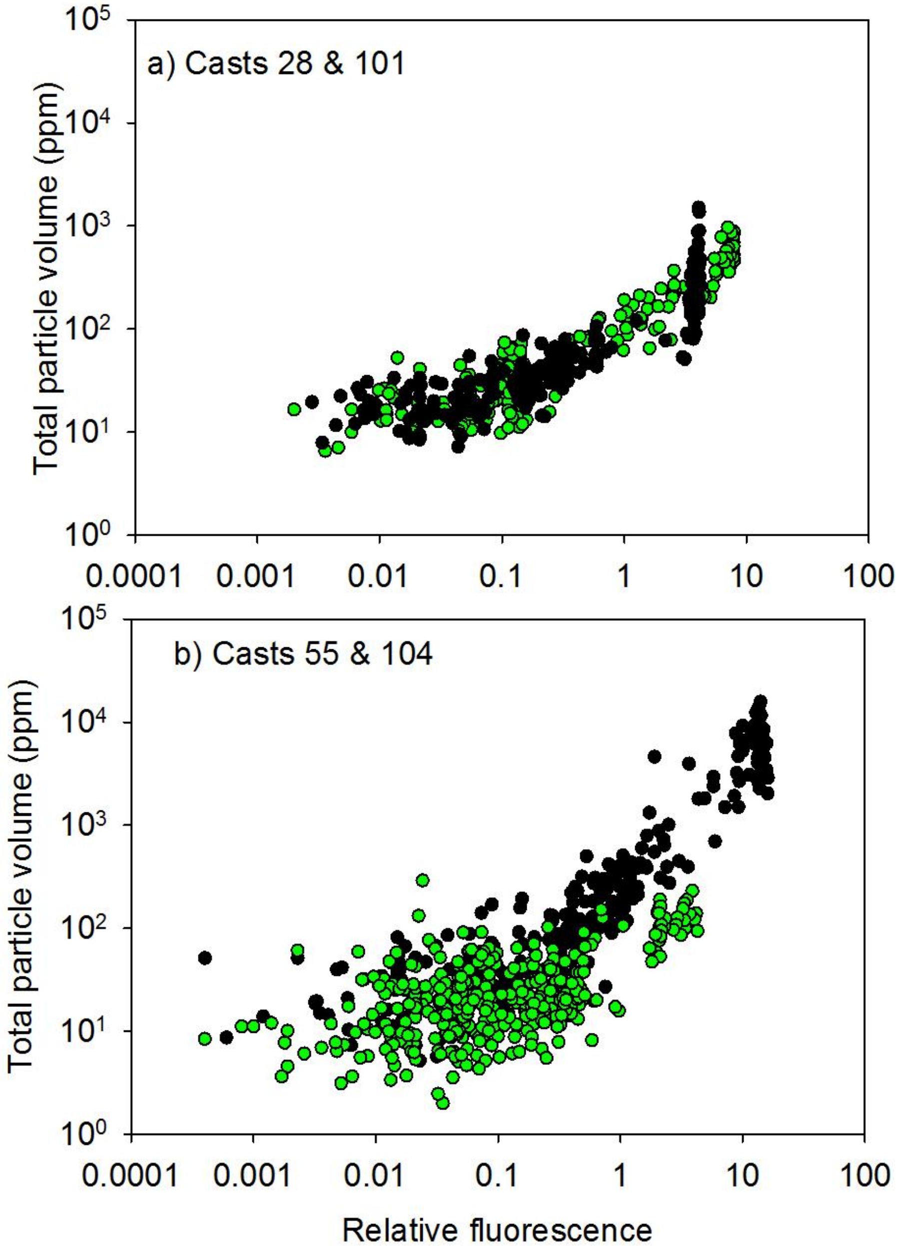

a) Casts 28 & 101
Total particle volume (ppm)
b) Casts 55 & 104
Total particle volume (ppm)
Relative fluorescence

Fig. 9

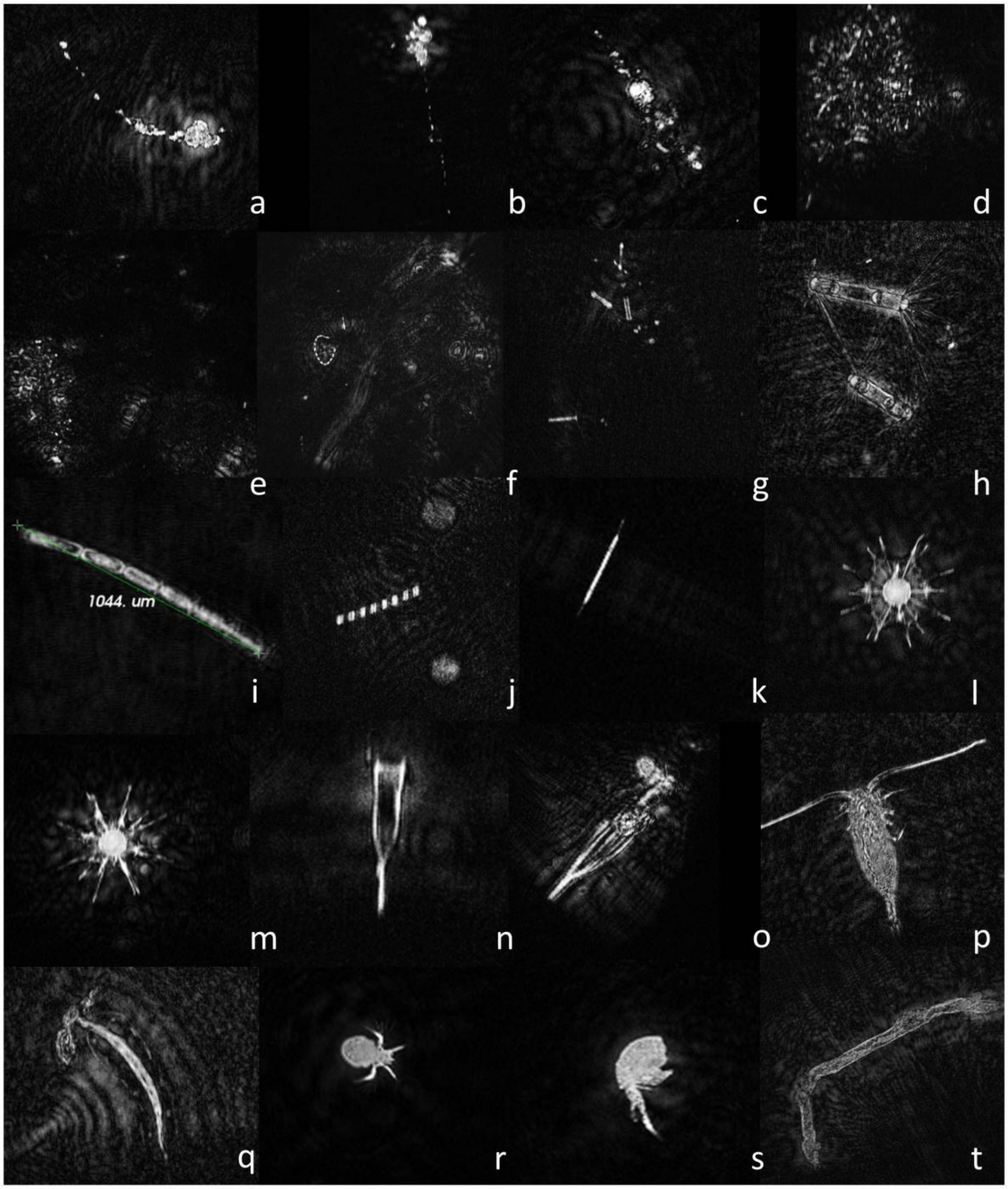

Fig. 10

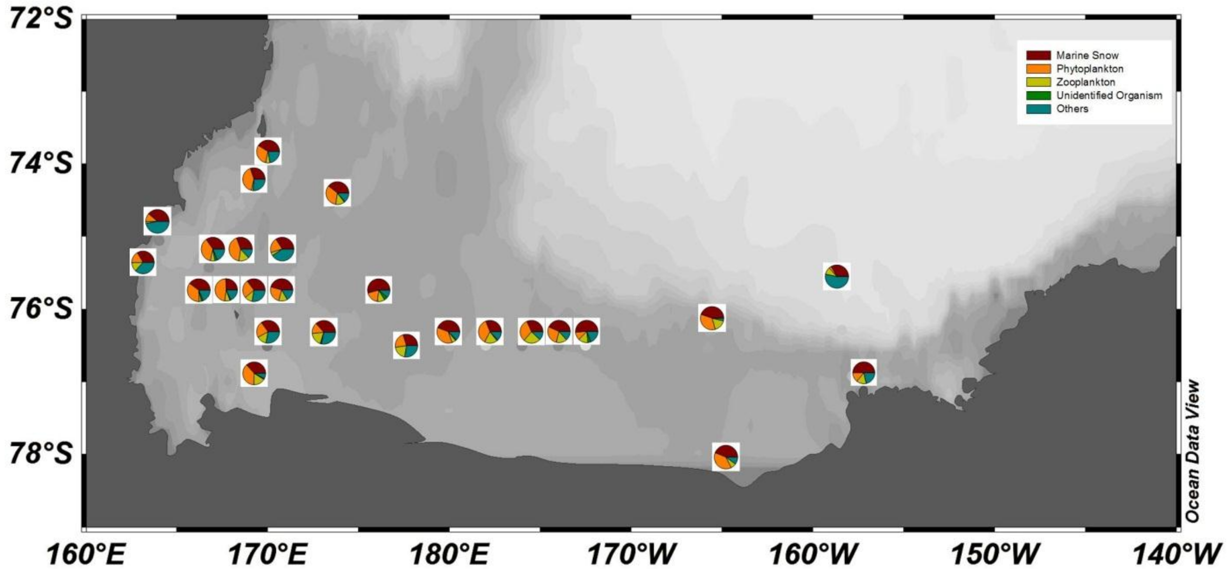
Marine Snow
Phytoplankton
Zooplankton
Unidentified Organism
Others
72°S
74°S
76°S
78°S
160°E
170°E
180°E
170°W
160°W
150°W
140°W
Ocean Data View

Fig. 11

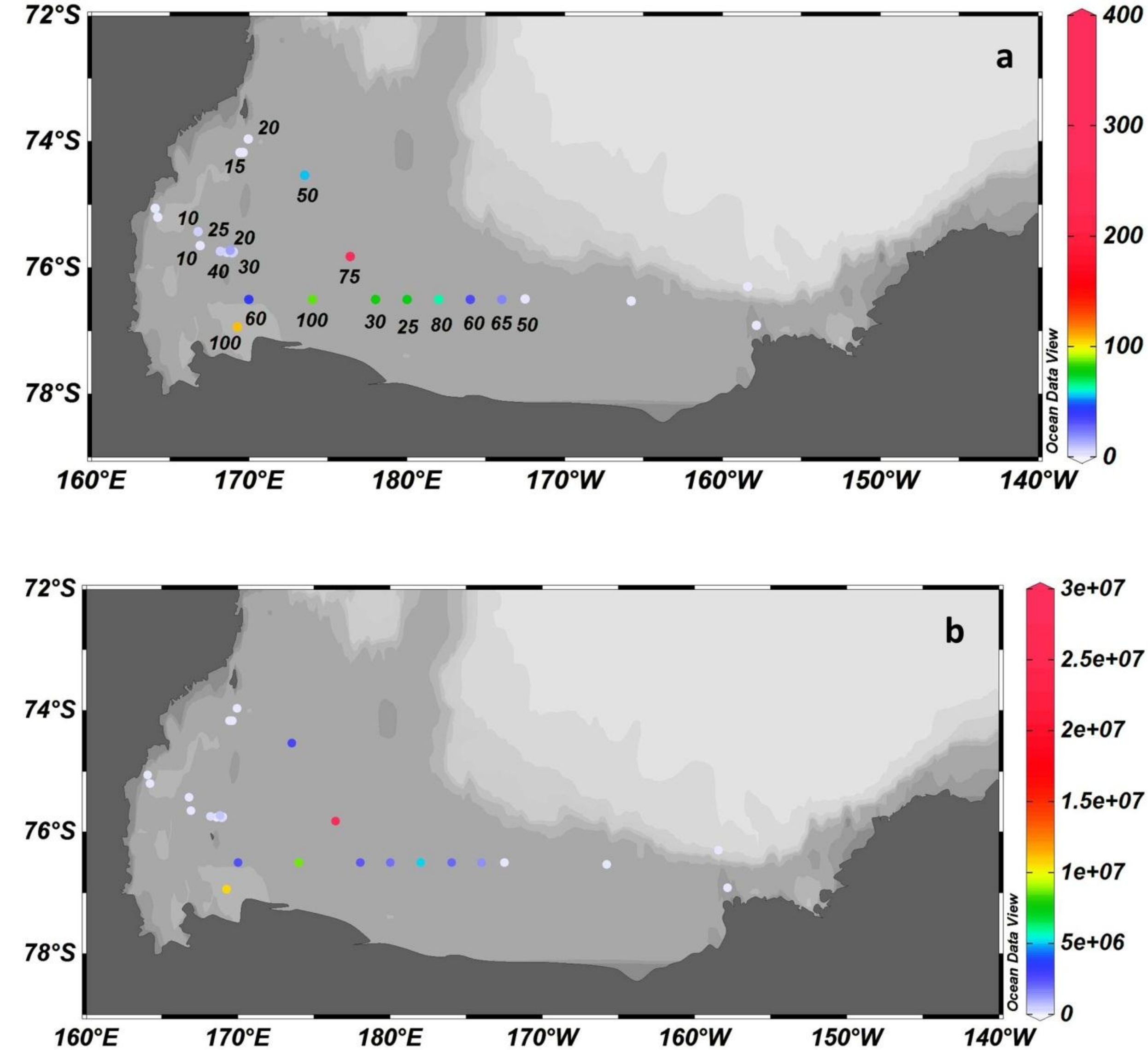
72°S
74°S
76°S
78°S
160°E
170°E
180°E
170°W
160°W
150°W
140°W
a
20
15
50
10
25
20
10
40
30
75
60
100
30
25
80
60
65
50
100
400
300
200
100
0
Ocean Data View
b
3e+07
2.5e+07
2e+07
1.5e+07
1e+07
5e+06
0

Fig. 12

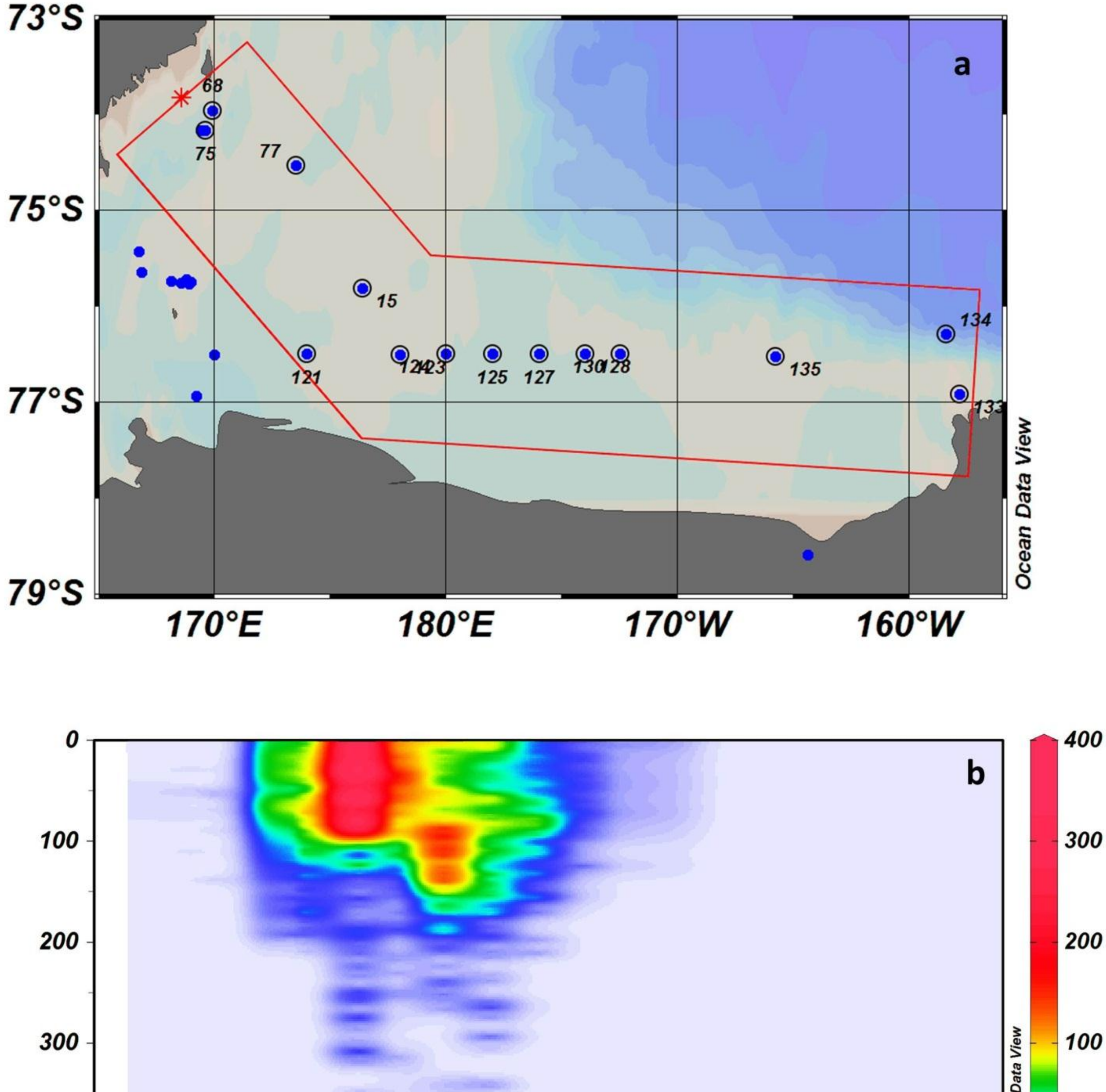

a
73°S
75°S
77°S
79°S
170°E
180°E
170°W
160°W
68
75
77
15
121
124
123
125
127
130
128
135
134
133
Ocean Data View
b
0
100
200
300
400
170°E
180°E
170°W
160°W
400
300
200
100
0
Ocean Data View

Fig. 13

514

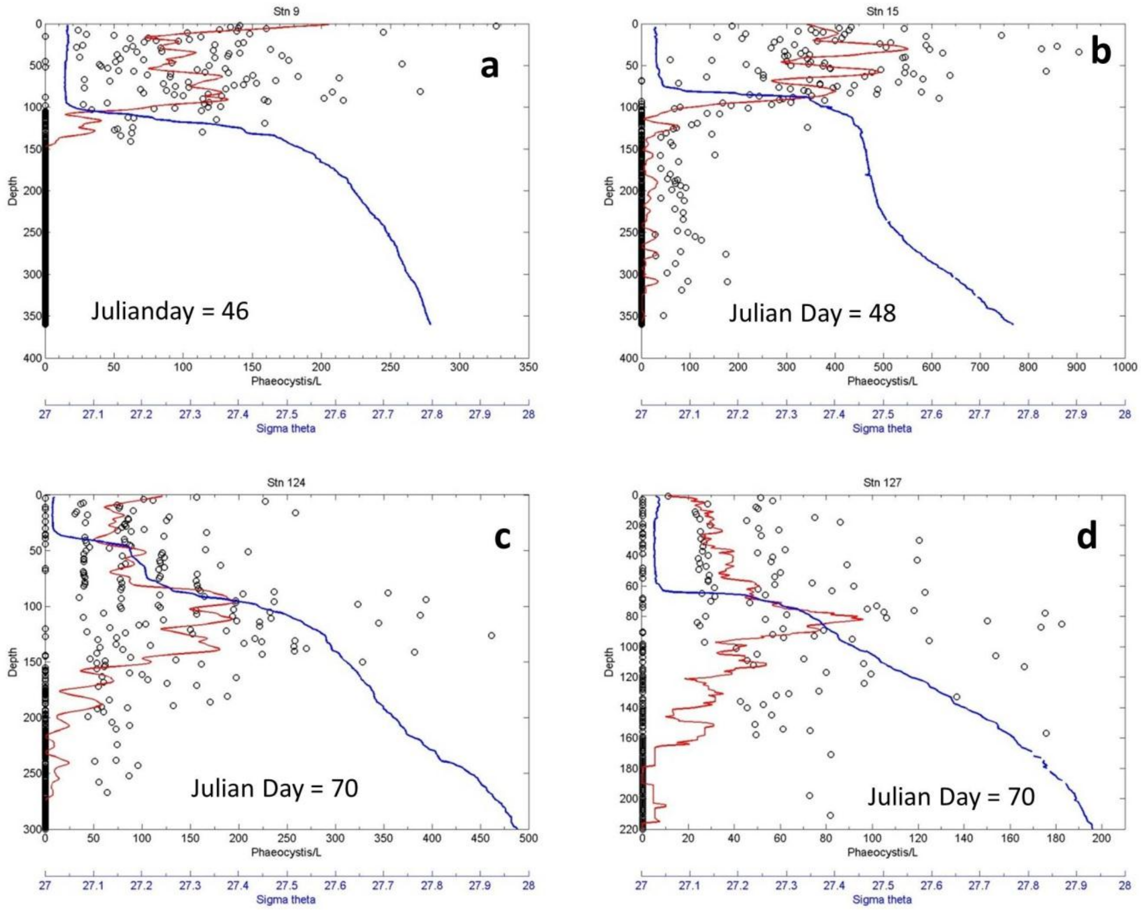
Stn 9
a
Julianday = 46
Depth
Phaeocystis/L
Sigma theta
Stn 15
b
Julian Day = 48
Depth
Phaeocystis/L
Sigma theta
Stn 124
c
Julian Day = 70
Depth
Phaeocystis/L
Sigma theta
Stn 127
d
Julian Day = 70
Depth
Phaeocystis/L
Sigma theta

Fig. 14